Published in final edited form as:
Small. 2012 July 23; 8(14): 2195–2202. doi:10.1002/smll.201102150.

The Role of Nanoscale Architecture in Supramolecular Templating of Biomimetic Hydroxyapatite Mineralization

Christina J. Newcomb[1], **Ronit Bitton**[2], **Yuri S. Velichko**[1], **Malcolm L. Snead**[3], and **Samuel I. Stupp**[*,1,2,4,5]

[1]Department of Materials Science and Engineering Northwestern University, Evanston, IL, USA

[2]The Institute for BioNanotechnology in Medicine, Northwestern University, Chicago, IL, USA

[3]The Center for Craniofacial Molecular Biology, CSA 142, Health Sciences Campus, Herman Ostrow School of Dentistry, University of Southern California, Los Angeles, CA, USA

[4]Department of Chemistry, Northwestern University, Evanston, IL, USA

[5]Department of Medicine, Northwestern University, Chicago, IL, USA

Abstract

Understanding and mimicking the hierarchical structure of mineralized tissue is a challenge in the field of biomineralization and is important for the development of scaffolds to guide bone regeneration. Bone is a remarkable tissue with an organic matrix comprised of aligned collagen bundles embedded with nanometer-sized inorganic hydroxyapatite (HAP) crystals that exhibit orientation on the macroscale. Hybrid organic-inorganic structures mimic the composition of mineralized tissue for functional bone scaffolds, but the relationship between morphology of the organic matrix and orientation of mineral is poorly understood. We report here the mineralization of supramolecular peptide amphiphile templates that are designed to vary in nanoscale morphology by altering the amino acid sequence. We found that one-dimensional cylindrical nanostructures directed the growth of oriented HAP crystals, while flatter nanostructures failed to guide the orientation found in biological systems. The geometric constraints associated with the morphology of the nanostructures may effectively control HAP nucleation and growth. Additionally, we explored the mineralization of macroscopically aligned bundles of the nanoscale assemblies to create hierarchically ordered scaffolds. Again, we found that only aligned gel templates of cylindrical nanostructures led to hierarchical control over hydroxyapatite orientation across multiple length scales as found in bone.

Keywords

biomineralization; hybrid materials; self-assembly; peptide amphiphile; biomimetic; hydroxyapatite

Introduction

Controlled organization of well-defined, bioinspired architectures across extended length scales using organic-inorganic hybrid materials is of great interest for applications in tissue regeneration.[1-5] In living organisms, cellular processes facilitate precise control over the formation of mineralized tissues that are comprised of both organic and inorganic

---

[*]Corresponding Author: Prof. Samuel I. Stupp, Northwestern University, Institute for BioNanotechnology in Medicine, 303 E Superior 11-123 Chicago, IL 60611, USA. s-stupp@northwestern.edu.

components. In mammalian bone, nanoscale inorganic carbonated hydroxyapatite (HAP) crystallites are crystallographically oriented with their c-axes parallel to the long axis of organic collagen fiber and hierarchically organized with collagen bundles across nano- and even macroscopic length scales.[6-8] Collagen itself contains multiple levels of hierarchy; it is comprised of high-aspect-ratio polypeptide triple helices approximately 1.25 nm in diameter that are staggered along their length and arranged into fibrils that are up to a few hundred nanometers in diameter and extend millimeters in length.[9] In an effort to mimic the composition of mineralized tissue in artificial systems, several organic templates have been investigated for their ability to nucleate biological minerals on the nanoscale, including self-assembled monolayers,[10, 11] biopolymers, and poly(amino acids).[12] However, most of these systems do not achieve nanoscale crystallographic alignment of HAP and therefore do not mimic the hierarchical structure of bone. Current techniques for producing hierarchical structures for mineralization at the macroscale include electrospinning,[13] directional freezing,[14] and biotemplating,[15, 16] however, organizing mineralized structures with oriented nucleation of HAP at the meso- and macroscopic length scales is difficult. The most successful mimics thus far include collagen, which has shown the ability to align HAP[17, 18] and has recently demonstrated the ability to create macroscopic domains of oriented, mineralized collagen by taking advantage of its liquid-crystalline behavior.[19] However, nucleation of oriented HAP over macroscopic scales has been difficult to achieve with synthetic templates. A synthetic approach is promising for use in bone scaffolds because it provides facile synthesis and affords better reproducibility compared with animal-derived proteins.

Peptide-based self-assembly is a powerful strategy for designing templates for biomineralization. Our group studies a class of molecules known as peptide amphiphiles (PAs) that contain a hydrophobic alkyl tail covalently attached to a peptide sequence. In an aqueous environment, the hydrophobic collapse of alkyl tails and high propensity of certain peptide sequences to form β-sheets yields high-aspect ratio supramolecular nanofibers.[20, 21] The supramolecular morphology of PA nanofibers can be controlled through the primary peptide sequence by regulation of intermolecular forces, i.e. hydrogen bonding strength, peptide chirality, and the distribution of electrostatic charge. For example, the amino acids in the domain closest to the alkyl tail have been shown to promote β-sheet hydrogen bonding along the long axis of the nanostructure and can be varied to control the molecular packing, and ultimately the nanostructure shape.[22-24] Alterations to the peptide sequence enable a variety of nanoscale morphologies including cylindrical fibers[25-27], twisted ribbons [28, 29], and flat belts.[24] PAs are versatile and highly tunable, as they can be designed with varying mechanical properties[22] and can be customized to include bioactive epitopes that are presented on their surface in high densities for cell signaling and applications in regenerative therapies. PAs have been designed for therapeutic applications in spinal cord injury,[30, 31] angiogenesis,[32-34] and regeneration of bone,[35] cartilage,[36] and enamel.[37, 38]

During formation of bone, osteoblast cells synthesize a self-assembled matrix within the extracellular space. Soluble macromolecules interact with the matrix to control mineral deposition, crystal habit, and orientation within a structural framework that acts a template for nucleation and growth of HAP.[39, 40] The extracellular matrix, which is responsible for templating HAP in mineralized tissues, contains one-dimensional, fiber-like nanostructures, thus making PA nanofibers attractive for exploring biomimetic mineralization. Recently, cylindrical assemblies of filamentous bacteriophage bearing acidic coat proteins have demonstrated oriented HAP mineralization.[16, 41] Also, have previously shown cylindrical PA nanofibers can act as an organic template for biomineralization in a two dimensional system, nucleating HAP crystals with the c-axis of the mineral oriented along the long axis of nanofibers.[25] Since phosphoproteins have been proposed to mediate collagen mineralization,[42] these PA molecules were designed to include a phosphorylated serine residue that resulted in accelerated kinetics of HAP crystallization as compared to non-phosphorylated controls. Mineralization was further demonstrated with this molecule in three-dimensional PA nanofiber gel networks using alkaline phosphatase (ALP) to harvest inorganic phosphate ions from β-glycerophosphate.[43] Although we have demonstrated the ability to nucleate oriented HAP using PA nanofibers, the role of molecular packing and intermolecular forces within the template to control crystal growth in inorganic-organic composite materials remains unclear. Furthermore, in our previous work mineralization was limited to orientationally isotropic systems and HAP alignment was only achieved locally on nanometer length scales.

Recently, our group has reported a technique to create highly aligned bundles of PA nanofibers, which could provide a means for forming hierarchical structures mimetic of bone.[44] Through the use of a thermal pathway, hydrated, three-dimensional monodomain gels with highly aligned bundles of PA nanofibers can be formed. The assembly mechanism proceeds by heating a solution of PA, creating large “plaque-like” bundles of the nanostructures, which break spontaneously into smaller one-dimensional bundles upon cooling. The resulting solution can form oriented, micron-sized domains upon gelling by the addition of counterions. In contrast to techniques such as directional freezing and electrospinning, which require the removal of solvent and high voltages that can be deleterious to cell survival,[14, 45] a solution of these supramolecular bundles can be seeded with cells after cooling and will form gels with oriented bundles of nanostructures over macroscopic lengths when drawn into a simple salt solution. These constructs can be used to mimic the organic component of bone, which is primarily composed of aligned collagen bundles approximately 100 nm in diameter.

In this study, we explore the ability of PA assemblies to guide HAP nucleation by varying the overall charge and propensity for β-sheet hydrogen bonding of the PA molecule. This system uniquely affords the molecular versatility to study HAP mineralization on high aspect ratio nanostructures with defined shapes. Furthermore, we explore HAP mineralization in three dimensional, aligned gels that could be used as cell scaffolds that offer the possibility to study cell response to anisotropic, mineralized constructs. These biomimetic, hybrid materials have potential for use in repair of bone fractures or defects, or could be integrated into a load bearing metallic implant[46].

Results and Discussion

We designed and synthesized three molecules, palmitoyl-VVVAAAEEE, (**PA 1**, Figure 1a) palmitoyl-VVAAEEE (**PA 2**, Figure 1b) and palmitoyl-VVAAEE (**PA 3**, Figure 1c), each containing glutamic acid residues, as proteins that engage in biological mineralization are often highly acidic and promote local supersaturation of calcium ions for nucleation of calcium phosphate.[42, 47] These PAs were also chosen because they form one-dimensional assemblies with distinct nanoscale morphologies and both **PA 1** and **PA 3** have been shown to easily form the novel monodomain gels recently reported by our group.[44] PA solutions were thermally treated at 80 °C for 30 minutes at 1% (w/v) in water at pH 7.4 and cooled to room temperature to keep conditions consistent with those used to form monodomain gels. To visualize the hydrated nanostructure, the heated and cooled solution was diluted to a concentration of 0.1% (w/v) and imaged by cryogenic transmission electron microscopy (cryo-TEM). **PA 1** contains four carboxyl groups and formed cylindrical nanofibers with a regular diameter of approximately 10 nm (Figure 1e). **PA 2** also contains four carboxyl groups, but the β-sheet sequence has lower propensity for hydrogen bonding and formed flat and twisted ribbon-like structures that were approximately 21 nm in width (Figure 1f). **PA 3** has the same VVAA peptide backbone as **PA 2**, but contains only two carboxyl groups, which reduces the electrostatic repulsion between molecules. This PA structure leads to assemblies with the shape of flat twisted ribbons approximately 30 nm in width (Figure 1g). Small angle X-ray scattering (SAXS) of 1% (w/v) solutions that were heated and cooled further confirmed the differences in the distribution of electron density within the nanostructures. **PA 1** demostrated a power-law dependence of q^{-1}, in the low q region indicative of rods, while **PA 3** adopted a q^{-2} dependence, indicating the presence of flat structures (Figure S1).[48] The low q range dependence in SAXS is intermediate between **PA 1** and **PA 3**, likely due to the narrower ribbon morphology. The reduced electrostatic repulsion among carboxylic acids at the terminus of **PA 3** compared to the other molecules may allow the molecules to pack more closely allowing for the wider, bilayer-like ribbon morphology. The narrower diameter of **PA 2** compared to **PA 3** is likely due to the increased electrostatic repulsion among headgroups, while the ribbon morphology is possibly dominated by the nature of the amino acid sequence closest to the alkyl tail.

Intermolecular β-sheet hydrogen bonding is crucial to promote the assembly of one-dimensional PA nanostructures.[22] To probe the nature of these interactions, the secondary structure of the assembled molecules was studied using circular dichroism. A typical protein β-sheet signature has a maximum of positive ellipticity at 195 nm indicative of a $\pi \rightarrow \pi^*$ transition and a minimum of negative ellipticity at 216 nm indicative of an $n \rightarrow \pi$ transition. The spectra from all three molecules revealed β-sheet character (Figure 1d). However, both **PA 1** and **PA 2**, which have equivalent charge and narrower one-dimensional nanostructures, were red-shifted compared to typical β-sheets seen in proteins (Figure S2). A red-shift in the signal has been shown to correlate with a strong twist in the β-sheet and has been attributed to polyvaline β-sheet structures.[49] As shown previously, the average red shift of **PA 2** is higher than **PA 1**, indicating increased β-sheet twisting when the molecule contains fewer valine residues, but equivalent charge.[22] In contrast, the maxima and minima of **PA 3**, which has less charge than the other molecules, exhibits a blue-shift that is likely indicative of planar and stacked β-sheets,[50] correlating with the flat, bilayer morphology that is observed in both cryogenic TEM and SAXS. These results suggest that electrostatic repulsion and chirality play a significant role in the template assembly.

To understand the relationship between the morphology of the PA template and the formation of HAP at early stages of crystallization at the nanoscale, we first evaluated PA mineralized in solution at 0.1% (w/v). For mineralization studies, inorganic phosphate was introduced through hydrolysis of an organic phosphate precursor, β-glycerophosphate, by the enzyme alkaline phosphatase (ALP). This method allowed enzyme-controlled delivery of inorganic phosphate in a time-resolved manner, avoiding homogeneous nucleation in solution.[43, 51] Cryo-TEM of these PA solutions revealed nucleation of mineral on the PA nanostructures following one hour of incubation at 37°C. The electron-dense mineral scatters electrons more than the PA nanostructures, resulting in increased contrast and revealing the inorganic component on the micrographs. In these images, we observe a nanostructure-dependent difference in the orientation of the HAP crystallites formed after this short period of time. The nanofibers of **PA 1** promoted control over mineral orientation (Figure 2a), while the nanostructures of **PA 2** and **PA 3** nucleated HAP crystallites with random orientation (Figure 2b, 2c). It is worthwhile noting that the overall lengths of the organic nanostructures in the micrographs demonstrating mineralization appear shorter. The presence of multivalent salts such as calcium, allows for the formation of ionic bridging between nanostructures. TEM preparation involved pipetting of the solution, which may break up large crosslinked domains into shorter nanostructures (Figure S3). Additionally, control samples containing no PA exhibited some spherical amorphous calcium phosphate, but no crystalline mineral was observed (Figure S4). At the timepoints chosen for these experiments, mineral with this spherical morphology was not observed in the presence of PA.

The crystallographic relationship between the organic and inorganic was investigated using selected area electron diffraction on unstained, drop-cast samples that were mineralized for four hours in solution at 37°C. HAP nucleation was confirmed for the **PA 1** template by the presence of reflections from the (002) and (004) crystal planes and the family of {211} crystal planes (Figure 2d, 2g), while **PA 2** (Figures 2e, 2h) and **PA 3** (Figures 2f, 2i) templates revealed (002) and {211} HAP reflections. **PA 1** nucleated mineral with the crystallographic c-axis aligned along the long axis of the nanostructure, similar to HAP crystal alignment in bone. The texture in both (002) and (004) HAP planes in the diffraction pattern (white arrowheads depict the arcs from the (002) reflection) indicates that the crystallites are oriented along the length of the nanostructure. A portion of un-mineralized organic template is indicated in Figure 2d with black arrows and the inorganic is indicated with arrowheads. Meanwhile, the mineral that was nucleated on the flatter nanostructures of **PA 2** and **PA 3** revealed no apparent texture in their electron diffraction patterns (Figures 2f, 2g), indicating a random orientation of the crystallites independent of overall charge or end-group chemistry. This evidence for morphology-dependent mineralization was further corroborated with additional cylindrical PA nanostructures that fit to a core-shell cylindrical model by SAXS (Figure S5) and flat belt-like nanostructures, which failed to show oriented mineral (Figure S6). A schematic depicting the mineral orientation with respect to the templates with different shapes can be found in Figure 3. This difference in template shape suggests that the cylindrical morphology is important nanoscale feature to obtain oriented mineral growth, as few organic templates other than collagen have the ability to control HAP nucleation on the nanoscale.[19]

We observed that the oriented growth of HAP mineral using supramolecular peptide amphiphile templates is dependent on template morphology. Factors including intermolecular forces and packing within the nanostructure, hydration of the peptides, and the dimensions of the template likely play roles in achieving directed HAP mineralization. First of all, the cylindrical nanofibers have diameters smaller than the width of the ribbon templates, and may provide a defined space for HAP to nucleate and grow preferentially along the principal axis of the assembly. In addition to a narrower diameter, the cylindrical nanofibers contain radially separated β-sheets resulting in less planar molecular packing and both a more hydrated environment and increased freedom of the headgroup. We demonstrated previously that the cylindrical PA nanofibers are internally well solvated,[52] which may afford greater accessibility of calcium ions to acidic residues and greater molecular motion to accommodate ion positions in the templated crystal. In contrast, the flatter PA assemblies that fail to orient HAP are likely less hydrated and the planar β-sheet signature seen from CD of **PA 3** suggests that the conformational freedom needed for oriented growth may be restricted. For example, mineralization of a self-assembled monolayer displaying carboxyl groups results in the formation of a “film” of HAP that lacks controlled nanoscale orientation with respect to the substrate.[53, 54] Interestingly, the morphology-dependent mineralization of the flat nanostructures of **PA 2** is maintained despite a twisted β-sheet conformation according to CD. In fact, recent studies of mineral-associated proteins such as osteopontin have been found to lack periodic structure and instead, the mineral formation is likely highly electrostatic with molecular disorder accommodating HAP growth,[55] indicating that the mobility of the peptides in the PA nanofiber may play a significant role in allowing for oriented growth of the crystal.

While these studies showed the potential for isotropic mineralization in solution, it was of great interest to create a unique hierarchical scaffold that can hierarchically template HAP appropriate for bone regeneration. Aligned, monodomain gels of **PA 1** and **PA 3** were prepared and mineralized to create macroscopically aligned hybrid constructs. A solution of PA was heated and ALP was incorporated into the PA solution after cooling to room temperature. This thermal treatment allows for the formation of micron-sized bundles, allowing for the formation of monodomain gels that were prepared from either **PA 1** or **PA 3** by drawing the solution into a mineralization solution containing $CaCl_2$, Tris-HCl and β-glycerophosphate. After incubating this gel for 24 hours at 37°C, mineral formation was readily visible on a macroscopic scale, as all of the monodomain gel samples containing ALP became opaque (Figures 4a,b). Additionally, the gels maintained an aligned architecture on the macroscopic length scale following addition of the enzyme and mineralization solution, as demonstrated by their birefringence in polarized light microscopy (Figures 3c,d). To evaluate the mineral phase, scanning electron microscopy (SEM) was performed on mineralized monodomain gels and inorganic mineral was found to be associated with the organic templates (Figures 4e,f). Energy dispersive X-ray spectroscopy (EDS) was used to identify the overall chemical composition of the inorganic phase (Figure 4g). **PA 1** and **PA 3** were found to contain calcium phosphate with Ca/P ratios of 1.4 ± 0.2 and 1.5 ± 0.2, respectively. These values were close to the stoichiometric ratio of Ca/P of HAP (1.67), but may indicate a mixture of additional polymorphs.

To further evaluate the polymorph and crystallographic orientation of the inorganic phase on a larger length scale, synchrotron X-ray fiber diffraction (XRD) was performed using a beam with a 200 μm diameter on hydrated monodomain gels. Diffraction was not observed for additional polymorphs of calcium phosphate following 24 hours of mineralization, similar to the electron diffraction data from PA mineralized in solution. Due to the propensity of the PA to form β-sheets, the XRD patterns from all of the monodomain gels revealed reflections for the spacing of adjacent β-strands (4.68Å).[56] Texture in the β-sheet spacing without addition of ALP is parallel to the long axis of the monodomain gel and is attributed to the macroscale alignment of the β-sheet hydrogen bonding that occurs along this axis (Figures 5a,b).[44] Mineralized gels exhibited d-spacings for the inorganic HAP ((002), {211}) (Figures 5c,d) and upon integration of the (002) ring from the XRD pattern for mineralized monodomain gels prepared from **PA 1**, it is clear that the HAP *c*-axis is oriented parallel to the β-sheet, and therefore parallel to the long axis of the monodomain gel (Figure 5e). The presence of a diffraction ring indicates that within the 200 μm area of the beam, some of the HAP crystals are not entirely oriented along the long axis of the gel. Overgrowth of the crystals that are no longer templated by the organic matrix may contribute to this observation. In contrast, the XRD pattern from mineral nucleated by monodomain gels of **PA 3**, which formed flat structures in solution, did not reveal any orientation as evidenced by an isotropic (002) ring (Figure 5f). These data demonstrate that the control over mineral orientation that was observed in solution for cylindrical nanostructures of **PA 1** translates to oriented, cylindrical bundles formed in monodomain gels. In contrast, similar monodomain gels comprised of flat nanostructures promoted the formation of randomly oriented mineral.

The protein-crystal interactions in mineralized tissues that allow for oriented growth of HAP have been somewhat controversial. Some investigators have speculated that the β-sheet secondary structure of proteins may provide a stereochemical match for crystallization of HAP.[57] It is interesting to note that all of the PA templates that were investigated exhibited a β-sheet secondary structure by CD. However distinct crystallographic orientation of HAP was only observed with **PA 1**, suggesting that if the β-sheet secondary structure is capable of providing a template for mineralization, a highly specific degree of twist and molecular spacing within the nanostructure is required. In fact, our supramolecular templates appear to support the flexible polyelectrolyte model, where the crystals are predominantly nucleated by electrostatics and molecular disorder assists in templating the mineral.[55]

Conclusions

We have demonstrated that the ability to nucleate oriented hydroxyapatite using a fibrous supramolecular template depends strongly on the details of its nanoscale architecture. Mineral oriented relative to the principal axis of the fibers as it occurs in mammalian bone were only nucleated on calcium binding nanostructures with curved, cylindrical architectures, and not on chemically similar ones with flat surfaces. When cylindrical nanostructures were part of a hierarchically aligned monodomain gel containing bundles of nanofibers, the capacity to nucleate oriented crystals over multiple length scales was maintained. The templates described here may also be interesting to investigate the role of alignment in cell signaling and preparation of therapeutic constructs to promote in vivo regeneration of mineralized tissues.

Experimental Section

Peptide amphiphile synthesis

PA molecules were synthesized using standard fluorenylmethyloxycarbonyl (Fmoc)-solid phase peptide chemistry on a CSBio CS136XT automated peptide synthesizer. Protected amino acids Fmoc-Val-OH, Fmoc-Ala-OH, and Fmoc-Glu(OtBu) were coupled on a pre-loaded Fmoc-Glu(OtBu) Wang resin for **PA 1** or a Fmoc-Rink amide resin for synthesis of **PA 2**. Fmoc deprotection was performed using 30% piperidine in dimethylformamide (DMF) and couplings were performed with 4 equivalents of protected amino acid or palmitic acid, 3.95 equivalents of 2-(1H-benzotriazol-1-YL)-1,1,2,2-tetramethyluronium hexafluorophosphate (HBTU), and 6 equivalents of diisopropylethylamine (DIEA) in DMF. PA molecules and protecting groups were cleaved from the resin using a mixture of 95% trifluoroacetic acid (TFA), 2.5% water, and 2.5% triisopropylsilane for three hours. TFA was removed using rotary evaporation. The product was recovered by precipitation with cold diethyl ether, dried under vacuum, and purified using preparative scale reverse phase high performance liquid chromatography (Varian). The molecules were purified in a mobile phase gradient of water and acetonitrile, each with 0.1% NH_4OH, and the product identity was confirmed with ESI mass spectrometry. Pure product-containing fractions were combined and lyophilized, then stored at −20 °C until use.

Mineralization of peptide amphiphiles

PA solutions were dissolved at 10 mg/mL in ultrapure water (18.2 MΩ·cm, Millipore) and adjusted to a pH of 7.4 using 1M NaOH. Samples were placed in an 80 °C water bath for 30 min then were allowed to cool to room temperature overnight. Stock solutions of 500 mM $CaCl_2$ (Sigma-Aldrich), 1M Tris HCl (EMD Chemicals) pH 7.4, 100 mM β-glycerol phosphate (Sigma-Aldrich), and 1 U/μL bacterial alkaline phosphatase (Fermentas Life Sciences) were used to mineralize PA in a solution with final concentrations of 1 mg/mL PA, 24 mM $CaCl_2$, 50 mM Tris HCl, 14.4 mM β-glycerophosphate, and 1 mU/μL ALP. The solution was incubated at 37°C until the desired timepoint.

For mineralization of monodomain gels, PA was dissolved at 13.3 mg/mL as described above. Samples were placed in an 80 °C water bath for 30 minutes and were allowed to equilibrate to room temperature overnight. The PA solution was combined with ALP (1 U/μL) to yield a final concentration of 10 mg/mL PA and 250 mU/μL ALP. Monodomain gels were formed by pipetting a solution of PA into a mineralization solution containing 24 mM $CaCl_2$, 50 mM Tris HCl (pH 7.4), and 14.4 mM β-glycerol phosphate. Monodomain gels were incubated at 37 °C in mineralization solution for 24 hours prior to analysis.

Circular Dichroism

Circular dichroism was performed on a Jasco J-815 spectrometer with a quartz cuvette with a path length of 1mm. A solution of 1% (w/v) heated and cooled PA was mixed with a $CaCl_2$ solution for a final $CaCl_2$ concentration of 20 mM and allowed to incubate at room temperature for 15 minutes. The sample was then diluted to 0.01% (w/v) with MilliQ water, vortexed, and added to the cuvette for the measurement at room temperature. The data was averaged over three spectra for each sample.

Transmission Electron Microscopy

Cryo-TEM and conventional TEM were performed on a JEOL 1230 microscope with an accelerating voltage of 100kV. For cryo-TEM, 300 mesh copper grids with a lacey carbon support (Electron Microscopy Sciences) were treated with air plasma for 20 seconds (Harrick Plamsa). 5μL of the sample was deposited on a grid, and the sample was blotted using a Vitrobot Mark IV (FEI) vitrification robot at 100% humidity. The samples were vitrified by plunging them into a liquid ethane reservoir, transferred to liquid nitrogen, placed into a Gatan 626 cryo-holder through a cryo-transfer stage, and imaged using a Gatan 831 CCD camera. For conventional TEM 5μL of PA solution was deposited on a 300 mesh copper TEM grid with a carbon support film (Electron Microscopy Sciences). Excess solution was wicked away with filter paper, the grid was allowed to dry at ambient temperature and samples were imaged with a Gatan 831 CCD camera. Selected area electron diffraction was performed on conventional TEM samples using the same instrument settings as described above.

Scanning Electron Microscopy

PA gels were briefly rinsed in deionized water, fixed in 2% glutaraldehyde in water for 20 minutes at room temperature and immersed in a graded ethanol series for dehydration. Upon dehydration in 100% ethyl alcohol, samples were dried at the critical point of CO_2 using a critical point dryer (Tousimis Samdri-795) to preserve the structure. Samples were mounted on SEM stubs using carbon adhesive cement (Electron Microscopy Sciences) and coated with 12 nm of osmium metal using an osmium plasma coater (Filgen, OPC-60A). Images were obtained using a Hitachi S-4800 FE-SEM secondary electron detector with an accelerating voltage of 5kV. EDS was performed using a silicon drift detector at a working distance of 10 mm. Data was collected and analyzed using Inca software and Ca/P ratios were averaged over 5 different areas of each sample.

X-ray diffraction

X-ray fiber diffraction was performed at the Advanced Photon Source using a bending magnet station (beamline 14BMC, Argonne National Laboratory, Argonne, IL). All data were obtained using a beam energy of 12.67 keV (wavelength: 0.979Å). Hydrated monodomain gels were mounted on a MicroLasso™ or MicroSieve™ (Electron Microscopy Sciences) and placed in the path of the X-ray beam. Diffraction patterns were obtained from various points along each sample and both background subtraction and azimuthal integration were performed using FIT2D software.

Small angle X-ray scattering

SAXS measurements were performed at the Advanced Photon Source at Argonne National Laboratory using an insertion device beamline 5-ID-D Dupont-Northwestern-Dow Collaborative Access team (DND-CAT). 1.5 mm quartz capillaries were filled with solutions of PA at 1% (w/v) in water. Using energy of 15 keV, that data was collected using a CCD detector to sample distance of 245 cm and an exposure time between 3-6 seconds. The scattering intensity was recorded with a q range of $0.008 < q < 0.25$ Å^{-1} where the wave vector q was defined as $q = (4\pi/\lambda)\sin(\theta/2)$ where θ is the scattering angle. Two-dimensional SAXS images were azimuthally averaged to produce one-dimensional intensity profiles using FIT2D. For background subtraction, scattering profiles were obtained for capillaries filled with solvent. No attempt was made to convert the units to an absolute scale.

Supplementary Material

Refer to Web version on PubMed Central for supplementary material.

Acknowledgments

This work was supported by the NIH, National Institute for Dental and Craniofacial Research (NIDCR) 2R01 DE015920-06.PA molecules were synthesized using facilities at Northwestern University Institute for BioNanotechnology in Medicine (IBNAM) Peptide Synthesis Core. SEM was performed at the EPIC facility of the NUANCE Center at Northwestern University, which is supported by NSF-NSEC, NSF-MRSEC, Keck Foundation, the State of Illinois, and Northwestern University. TEM and electron diffraction were performed at the Northwestern Biological Imaging Facility, which is generously supported by the NU Office for Research. Use of the Advanced Photon Source was supported by the U.S. DOE, Basic Energy Sciences, and Office of Science under contract number DE-AC02-06CH11357. Use of the BioCARS Sector 14 was supported by the NIH and National Center for Research Resources RR007707.The authors are grateful to Steven Weigand for assistance with SAXS experiments and Guy Macha and Vukica Srajer for assistance with XRD. The authors are also grateful for invaluable discussion and suggestions from Liam Palmer, John Matson, Honggang Cui, and Matthew Webber.

References

1. Stupp SI, Braun PV. Molecular manipulation of microstructures: biomaterials, ceramics, and semiconductors. Science. 1997; 277(5330):1242–8. [PubMed: 9271562]
2. Place ES, Evans ND, Stevens MM. Complexity in biomaterials for tissue engineering. Nature Mater. 2009; 8(6):457–70. [PubMed: 19458646]
3. Kretlow JD, Mikos AG. Review: mineralization of synthetic polymer scaffolds for bone tissue engineering. Tissue Eng. 2007; 13(5):927–38. [PubMed: 17430090]
4. Müller-Mai CM, Stupp SI, Voigt C, Gross U. Nanoapatite and organoapatite implants in bone: histology and ultrastructure of the interface. J Biomed Mater Res. 1995; 29(1):9–18. [PubMed: 7713964]
5. Boyd N, Boyd R, Simon GP, Nisbet DR. Synthetic Multi-level Matrices for Bone Regeneration. J. Tiss. Eng. Reg. Med. 2011; 2:99–122.
6. Weiner S, Wagner HD. The Material Bone: Structure-Mechanical Function Relations. Annu. Rev. Mater. Sci. 1998; 28:271–298.
7. Palmer LC, Newcomb CJ, Kaltz SR, Spoerke ED, Stupp SI. Biomimetic systems for hydroxyapatite mineralization inspired by bone and enamel. Chem. Rev. 2008; 108(11):4754–83. [PubMed: 19006400]
8. Sanchez C, Arribart H, Guille MMG. Biomimetism and bioinspiration as tools for the design of innovative materials and systems. Nature Mater. 2005; 4(4):277–88. [PubMed: 15875305]
9. Miller A, Parker SB. Collagen: the organic matrix of bone. Philos. Trans. R. Soc. Lond., B, Biol. Sci. 1984; 304(1121):455–77. [PubMed: 6142488]
10. Dey A, Bomans PHH, Müller FA, Will J, Frederik PM, de With G, Sommerdijk NAJM. The role of prenucleation clusters in surface-induced calcium phosphate crystallization. Nature Mater. 2010; 9:1010–1014. [PubMed: 21076415]
11. Aizenberg J, Muller DA, Grazul JL, Hamann DR. Direct fabrication of large micropatterned single crystals. Science. 2003; 299(5610):1205–8. [PubMed: 12595685]
12. Bradley J, Bridgland L, Colyer D, Duer M, Friscic T, Gallagher J, Reid D, Skepper J, Trasler C. NMR of Biopolymer-Apatite Composites: Developing a Model of the Molecular Structure of the Mineral-Matrix Interface in Calcium Phosphate Biomaterials. Chem. Mater. 2010; 22:6109–6116.
13. Zhang Y, Venugopal JR, El-Turki A, Ramakrishna S, Su B, Lim CT. Electrospun biomimetic nanocomposite nanofibers of hydroxyapatite/chitosan for bone tissue engineering. Biomaterials. 2008; 29(32):4314–22. [PubMed: 18715637]

14. Zhang H, Hussain I, Brust M, Butler M, Rannard S, Cooper A. Aligned two-and three-dimensional structures by directional freezing of polymers and nanoparticles. Nature Mater. 2005; 4:787–793. [PubMed: 16184171]
15. Sotiropoulou S, Sierra-Sastre Y, Batt C. Biotemplated Nanostructured Materials†. Chem. Mater. 2008; 20:821–834.
16. Wang F, Cao B, Mao C. Bacteriophage Bundles with Pre-Aligned Ca Initiate the Oriented Nucleation and Growth of Hydroxylapatite. Chem. Mater. 2010; 22(12):3630–3636. [PubMed: 20802794]
17. Deshpande AS, Beniash E. Bio-inspired Synthesis of Mineralized Collagen Fibrils. Cryst. Growth Des. 2008; 8(8):3084–3090.
18. Olszta MJ, Cheng X, Jee SS, Kumar R, Kim Y-Y, Kaufman MJ, Douglas EP, Gower LB. Bone structure and formation: A new perspective. Mat. Sci. Eng. R. 2007; 58:77–116.
19. Nassif N, Gobeaux F, Seto J, Belamie E, Davidson P, Panine P, Mosser G, Fratzl P, Guille M. Self-Assembled Collagen– Apatite Matrix with Bone-like Hierarchy. Chem. Mater. 2010; 22:3307–3309.
20. Cui H, Webber MJ, Stupp SI. Self-assembly of peptide amphiphiles: From molecules to nanostructures to biomaterials. Biopolymers. 2010; 94(1):1–18. [PubMed: 20091874]
21. Webber MJ, Kessler JA, Stupp SI. Emerging peptide nanomedicine to regenerate tissues and organs. J. Intern. Med. 2010; 267(1):71–88. [PubMed: 20059645]
22. Pashuck ET, Cui H, Stupp SI. Tuning Supramolecular Rigidity of Peptide Fibers through Molecular Structure. J. Am. Chem. Soc. 2010; 132(17):6041–6046. [PubMed: 20377229]
23. Paramonov S, Jun H, Hartgerink J. Self-assembly of peptide-amphiphile nanofibers: The roles of hydrogen bonding and amphiphilic packing. J. Am. Chem. Soc. 2006; 128(22):7291–7298. [PubMed: 16734483]
24. Cui H, Muraoka T, Cheetham A, Stupp S. Self-Assembly of Giant Peptide Nanobelts. Nano. Lett. 2009; 9(3):945–951. [PubMed: 19193022]
25. Hartgerink JD, Beniash E, Stupp SI. Self-assembly and mineralization of peptide-amphiphile nanofibers. Science. 2001; 294(5547):1684–8. [PubMed: 11721046]
26. Muraoka T, Koh C-Y, Cui H, Stupp SI. Light-triggered bioactivity in three dimensions. Angew. Chem. Int. Ed. Engl. 2009; 48(32):5946–9. [PubMed: 19582745]
27. Cui H, Pashuck ET, Velichko YS, Weigand SJ, Cheetham AG, Newcomb CJ, Stupp SI. Spontaneous and x-ray-triggered crystallization at long range in self-assembling filament networks. Science. 2010; 327(5965):555–9. [PubMed: 20019248]
28. Pashuck ET, Stupp SI. Direct observation of morphological transformation from twisted ribbons into helical ribbons. J. Am. Chem. Soc. 2010; 132(26):8819–21. [PubMed: 20552966]
29. Goldberger JE, Berns E, Bitton R, Newcomb CJ, Stupp SI. Electrostatic Control of Bioactivity. Angew. Chem. 2011; 50:6292–6295. [PubMed: 21626619]
30. Silva GA, Czeisler C, Niece KL, Beniash E, Harrington DA, Kessler JA, Stupp SI. Selective differentiation of neural progenitor cells by high-epitope density nanofibers. Science. 2004; 303(5662):1352–5. [PubMed: 14739465]
31. Tysseling-Mattiace VM, Sahni V, Niece KL, Birch D, Czeisler C, Fehlings MG, Stupp SI, Kessler JA. Self-assembling nanofibers inhibit glial scar formation and promote axon elongation after spinal cord injury. J Neurosci. 2008; 28(14):3814–23. [PubMed: 18385339]
32. Rajangam K, Behanna HA, Hui MJ, Han X, Hulvat JF, Lomasney JW, Stupp SI. Heparin binding nanostructures to promote growth of blood vessels. Nano. Lett. 2006; 6(9):2086–2090. [PubMed: 16968030]
33. Webber M, Han X, Prasanna-Murthy SN, Rajangam K, Stupp SI, Lomasney JW. Capturing the stem cell paracrine effect using heparin-presenting nanofibres to treat cardiovascular diseases. J. Tiss. Eng. Reg. Med. 2010; 4:600–610.
34. Webber MJ, Tongers J, Newcomb CJ, Marquardt K-T, Bauersachs J, Losordo DW, Stupp SI. Supramolecular nanostructures that mimic VEGF as a strategy for ischemic tissue repair. Proc. Natl. Acad. Sci. USA. 2011

35. Mata A, Geng Y, Henrikson KJ, Aparicio C, Stock SR, Satcher RL, Stupp SI. Bone regeneration mediated by biomimetic mineralization of a nanofiber matrix. Biomaterials. 2010; 31(23):6004–6012. [PubMed: 20472286]
36. Shah RN, Shah NA, Del Rosario Lim MM, Hsieh C, Nuber G, Stupp SI. Regenerative Medicine Special Feature: Supramolecular design of self-assembling nanofibers for cartilage regeneration. Proc. Natl. Acad. Sci. USA. 2010
37. Huang Z, Sargeant T, Hulvat J, Mata A, Bringas P, Koh C, Stupp S, Snead M. Bioactive Nanofibers Instruct Cells to Proliferate and Differentiate During Enamel Regeneration. J Bone Miner Res. 2008
38. Huang Z, Newcomb CJ, Bringas P, Stupp SI, Snead ML. Biological synthesis of tooth enamel instructed by an artificial matrix. Biomaterials. 2010; 31(35):9202–11. [PubMed: 20869764]
39. Veis A. Mineralization in organic matrix frameworks. Rev Mineral Geochem. 2003; 54:249–289.
40. Olszta MJ, Cheng X, Jee SS, Kumar R, Kim Y-Y, Kaufman MJ, Douglas EP, Gower LB. Bone structure and formation: A new perspective. Mat Sci Eng R. 2007; 58:77116.
41. He T, Abbineni G, Cao B, Mao C. Nanofibrous Bio-inorganic Hybrid Structures Formed Through Self-Assembly and Oriented Mineralization of Genetically Engineered Phage Nanofibers. Small. 2010; 6(20):2230–2235. [PubMed: 20830718]
42. George A, Veis A. Phosphorylated proteins and control over apatite nucleation, crystal growth, and inhibition. Chem. Rev. 2008; 108(11):4670–93. [PubMed: 18831570]
43. Spoerke ED, Anthony SG, Stupp SI. Enzyme Directed Templating of Artificial Bone Mineral. Adv. Mater. 2009; 21(4):425–430. [PubMed: 22068437]
44. Zhang S, Greenfield MA, Mata A, Palmer LC, Bitton R, Mantei JR, Aparicio C, de la Cruz MO, Stupp SI. A self-assembly pathway to aligned monodomain gels. Nature Mater. 2010; 9:594–601. [PubMed: 20543836]
45. Townsend-Nicholson A, Jayasinghe SN. Cell electrospinning: a unique biotechnique for encapsulating living organisms for generating active biological microthreads/scaffolds. Biomacromolecules. 2006; 7(12):3364–9. [PubMed: 17154464]
46. Sargeant TD, Guler MO, Oppenheimer SM, Mata A, Satcher RL, Dunand DC, Stupp SI. Hybrid bone implants: Self-assembly of peptide amphiphile nanofibers within porous titanium. Biomaterials. 2008; 29(2):161–171. [PubMed: 17936353]
47. Weiner S, Hood L. Soluble protein of the organic matrix of mollusk shells: a potential template for shell formation. Science. 1975; 190(4218):987–9. [PubMed: 1188379]
48. Glatter, O.; Kratky, O. Small Angle X-ray Scattering. Academic Press; 1982.
49. Manning MC, Illangasekare M, Woody RW. Circular dichroism studies of distorted alpha-helices, twisted beta-sheets, and beta turns. Biophys.Chem. 1988; 31(1-2):77–86. [PubMed: 3233294]
50. Cort J, Liu Z, Lee G, Harris S, Prickett K, Gaeta L, Andersen N. β-Structure in Human Amylin and 2 Designer β-Peptides: CD and NMR Spectroscopic Comparisons Suggest Soluble β-Oligomers and the Absence of Significant Populations of β-Strand Dimers Biochem. Biophys. Res. Commun. 1994; 204(3)
51. Gungormus M, Fong H, Kim IW, Evans JS, Tamerler C, Sarikaya M. Regulation of in vitro calcium phosphate mineralization by combinatorially selected hydroxyapatite-binding peptides. Biomacromolecules. 2008; 9(3):966–73. [PubMed: 18271563]
52. Tovar JD, Claussen RC, Stupp SI. Probing the interior of peptide amphiphile supramolecular aggregates. J. Am. Chem. Soc. 2005; 127(20):7337–45. [PubMed: 15898782]
53. Toworfe G, Composto R, Shapiro I, Ducheyne P. Nucleation and growth of calcium phosphate on amine-, carboxyl-and hydroxyl-silane self-assembled monolayers. Biomaterials. 2006; 27(4)
54. Tarasevich B, Chusuei C, Allara D. Nucleation and growth of calcium phosphate from physiological solutions onto self-assembled templates by a solution-formed nucleus mechanism. J. Phys. Chem. B. 2003; 107(38):10367–10377.
55. Hunter GK, O'Young J, Grohe B, Karttunen M, Goldberg HA. The Flexible Polyelectrolyte Hypothesis of Protein–Biomineral Interaction. Langmuir. 2010; 26(24):18639–18646. [PubMed: 20527831]
56. Sunde M, Blake C. The structure of amyloid fibrils by electron microscopy and X-ray diffraction. Adv. Protein Chem. 1997; 50:123–59. [PubMed: 9338080]

57. Addadi L, Weiner S. Interactions between acidic proteins and crystals: stereochemical requirements in biomineralization. Proc. Natl. Acad. Sci. USA. 1985; 82(12):4110–4. [PubMed: 3858868]

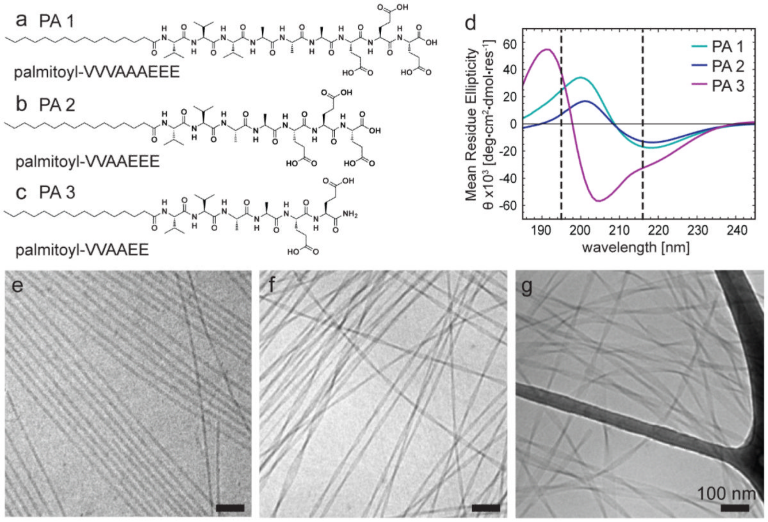

Figure 1.

Chemical structures of (a) PA 1 (b) PA 2 (c) PA 3 and (d) circular dichroism of these molecules demonstrating their β-sheet character. (e, f, g) Cryogenic transmission electron microscopy (TEM) of PA 1, PA 2, and PA 3 nanostructures in water after heating and cooling at 0.1% (w/v). PA 1 forms cylindrical nanostructures while PA 2 and PA 3 form twisted ribbon-like morphologies. Note that the grid bar is visible in panel (g). Scalebars: 100 nm.

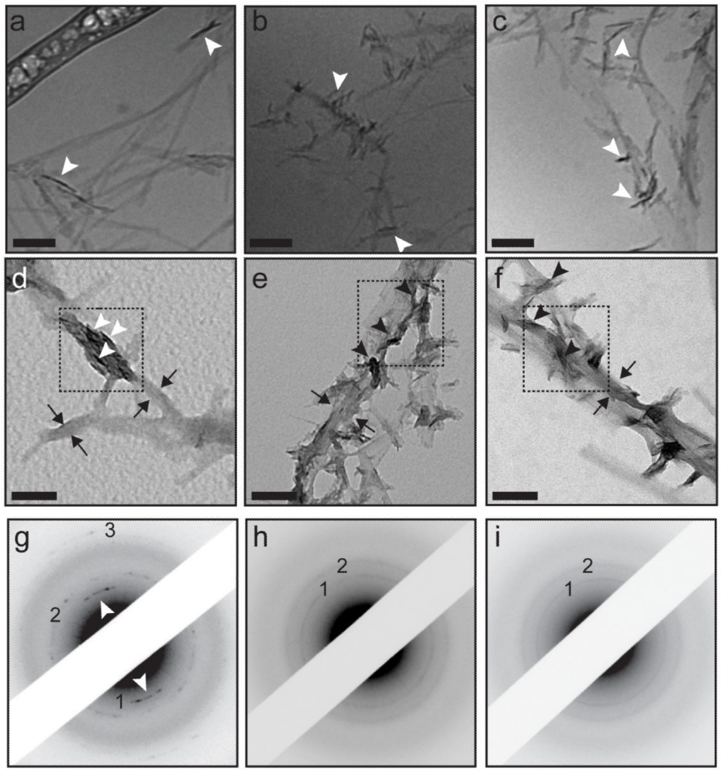

Figure 2.

Characterization of PA that has been mineralized in solution. Cryogenic transmission electron microscopy of (a) PA 1, (b) PA 2 and (c) PA 3 following one hour of mineralization. Unstained, drop-cast TEM images of a mineralized solution containing (d) PA 1, (e) PA 2 and (f) PA 3 following four hours of mineralization. Arrows indicate the location of the organic template and arrowheads indicate the position of inorganic crystals. The selected area electron diffraction (SAED) patterns corresponding to the areas within the dotted lines in (d-f) are shown for (g) PA 1, (h) PA 2, and (i) PA 3. The TEM and SAED patterns show that PA 1 is competent in nucleating oriented HAP while PA 2 and PA 3 nucleate randomly oriented HAP. Arrowheads indicate the oriented (002) reflection. (1: (002), 2:{211}, 3: (004)) Scalebars: 100 nm.

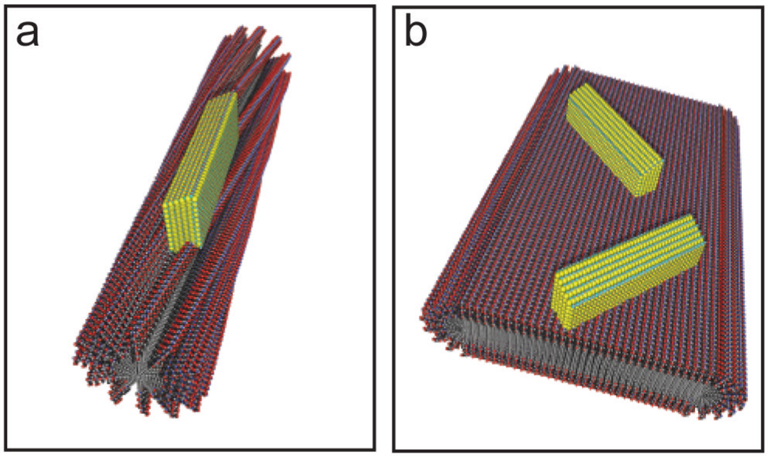

Figure 3.

A schematic showing the possible organic-inorganic relationship at the nanoscale. (a) A PA with a cylindrical morphology demonstrating crystal growth of the HAP c-axis down the long axis of the template. (b) A PA with a flat ribbon or bilayer-like morphology nucleating HAP with random crystallite orientations.

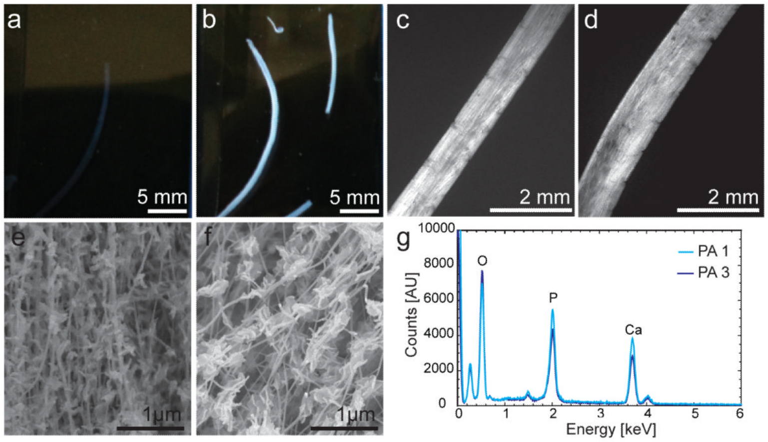

Figure 4.

A representative image of monodomain gels after 24 hours of mineralization (a) in the absence of ALP and (b) in the presence of ALP. Polarized light microscopy reveals global alignment in both (c) PA 1 and (d) PA 3 prior to mineralization, but following addition of ALP. Scanning electron microscopy of (e) PA 1 and (f) PA 3 show the presence of mineral associated with nanofibers and (g) energy dispersive spectroscopy demonstrates the presence of calcium phosphate in both samples.

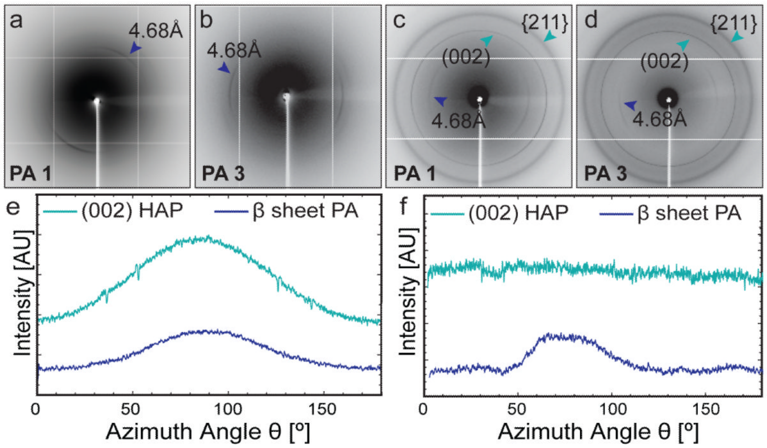

Figure 5.

Two-dimensional X-ray fiber diffraction (XRD) patterns from hydrated monodomain gels of PA 1 and PA 3 following 24 hours of mineralization (a,b) without ALP and (c,d) with ALP. The 4.68 Å reflection reflection corresponds to a regular β-sheet spacing from the PA fibers and both the (002) and {211} reflections from HAP are observed in samples where ALP is added. A plot of intensity vs. azimuthal angle around the XRD pattern shows the presence of oriented (002) arcs from HAP along the long axis of the monodomain gel of (e) PA1 and no orientation is observed in the case of (f) PA 3.